Strain dependence of band gaps and exciton energies in pure and mixed transition-metal dichalcogenides

Rodrick Kuate Defo,[1] Shiang Fang,[1] Sharmila N. Shirodkar,[2] Georgios A. Tritsaris,[2]
Athanasios Dimoulas,[3] and Efthimios Kaxiras[1,2]

[1]*Department of Physics, Harvard University, Cambridge, Massachusetts 02138, USA*
[2]*John A. Paulson School of Engineering and Applied Sciences, Harvard University, Cambridge, Massachusetts 02138, USA*
[3]*Institute of Nanoscience and Nanotechnology, National Center for Scientific Research Demokritos, 15310, Aghia Paraskevi, Athens, Greece*

(Received 6 June 2016; revised manuscript received 30 August 2016; published 27 October 2016)

The ability to fabricate 2D device architectures with desired properties, based on stacking of weakly (van der Waals) interacting atomically thin layers, is quickly becoming reality. In order to design ever more complex devices of this type, it is crucial to know the precise strain and composition dependence of the layers' electronic and optical properties. Here, we present a theoretical study of these dependences for monolayers with compositions varying from pure MX_2 to the mixed MXY, where $M =$ Mo, W and $X,Y =$ S, Se. We employ both density-functional-theory and GW calculations, as well as values of the exciton binding energies based on a self-consistent treatment of dielectric properties, to obtain the band gaps that correspond to optical or transport measurements; we find reasonable agreement with reported experimental values for the unstrained monolayers. Our predictions for the strain-dependent electronic properties should be a useful guide in the effort to design heterostructures composed of these layers on various substrates.

DOI: 10.1103/PhysRevB.94.155310

I. INTRODUCTION

Interest in 2D materials, originally sparked by the discovery of graphene, has been invigorated with the advent of single layers that exhibit semiconducting properties. Transition metal dichalcogenides (TMDCs, composition: MX_2, where $M=$ transition metals like Nb, Ta, Mo, W, Ti, and $X=$ chalcogens like S, Se, Te) are a particularly attractive class of semiconducting layered materials because their electronic and optical properties can be manipulated by chemical substitutions as well as by the number of layers and other structural features (stacking sequences and polytypes). Moreover, TMDCs exhibit unconventional phenomena such as topological superconductivity [1] and charge density waves [2] and have found widespread applications in varied areas like lubrication [3], catalysis [4], photovoltaics [5], and optoelectronics [6]. The range of possible applications grows enormously by considering heterostructures composed of various stacking orders and relative orientations of the single layers. To mention but a few examples, TMDCs can complement graphene in optoelectronic or energy harvesting applications requiring thin transparent semiconductors [7]; MoS_2/graphene heterostructures have already been fabricated and applied to energy harvesting with a photogain of over 10^8 [8] and to nonvolatile memory cells [9]; light emitting diodes have been constructed based on heterostructures of hexagonal boron nitride, silicon dioxide, silicon, graphene, WSe_2, and MoS_2 [10].

In the applications mentioned, variable composition and strain-induced effects could make a significant difference on the electronic and structural properties of the monolayer. Even allowing for the fact that the van der Waals (vdW) coupling between layers is weaker than covalent bonding, their interaction is non-negligible as the dependence of the electronic features on the number of layers indicates. In addition, controlled changes in the chemical composition, enabled by recent molecular beam epitaxy (MBE) growth of TMDCs [11,12], suggest that strain can be an inherent feature of each layer in a heterostructure. Investigations of strain effects have revealed a transition from a direct to an indirect band gap in the monolayer TMDCs [13,14] and metallic behavior for very large strains of ∼10% [13,15]. More pertinently, valley drift has been predicted under application of strain in MoS_2 [16], as well as a shift of the electron and hole band edges due to uniform strain [17], relevant to applications in photovoltaic devices or the creation of long-lived indirect excitons. The effect of twist angle on the band structure of bilayer MoS_2 has also been investigated and shown to induce widening of the band gap with twist angle due to modulation of the interlayer coupling [18]. The effect on the electronic properties of monolayer MoS_2 supported or suspended by a silicon substrate has also been examined [19] as well as the thickness dependence of electronic properties of WSe_2 [20]. Composition also plays an important role in the electronic properties of monolayers. For instance, temperature and the value of x in the formula $Mo_{1-x}W_xTe_2$ determine the relative stability of the H or T′ phases [21], the former being semiconducting and the latter semimetallic [22,23]. Further, the choice of chalcogen influences the piezoelectric properties of the H phase TMDC monolayers [24].

We present here an investigation of strain effects on the electronic and optical properties of the common TMDC materials MoS_2, $MoSe_2$ and WS_2, WSe_2 and their mixed variants, MoSSe, WSSe. The latter two structures do not as yet exist but are interesting limiting cases of compositional variation. Moreover, such structures could even be created, in principle, by recently developed MBE techniques [11,12], especially if a polar substrate were to be used. Such polar structures are interesting because they open the possibility of creating TMDC layers with inherent strain or polar character. Our results extend earlier work [14–17,25,26] in important ways: They provide a comprehensive discussion of the influence of strain on the dielectric function and hence the optical behavior of common TMDCs and their mixed variants, and they give a detailed account of how different components (dielectric constant,

 ©2016 American Physical Society

electron and hole effective masses, exciton binding energies) contribute to the overall changes in electronic structure induced by strain. In this sense, the present results offer a broad basis for designing heterostructures based on pure and mixed-character TMDCs with desirable optoelectronic properties.

II. COMPUTATIONAL METHODS

We performed first-principles density functional theory (DFT) calculations for structural optimization using the GPAW package [27–29], which is a grid-based approach employing the projected augmented-wave method [30]. For the exchange-correlation energy of electrons we use the generalized gradient approximation (GGA), as parametrized by Perdew, Burke, and Erzenhof (PBE) [31]. A vacuum of 15 Å separating the adjacent periodic images along the direction perpendicular to the plane was employed to simulate an isolated 2D planar sheet. The atomic positions were relaxed until the magnitude of Hellmann-Feynman forces was smaller than 0.01 eV/Å on each atom. The wave functions were expanded in a plane wave basis with a cutoff energy of 400 eV, and a zone-centered grid of $24 \times 24 \times 1$ points was used for integrations in k space for both structural and excited-state calculations.

We carried out GW calculations for MoS_2 as the benchmark compound to establish highly converged values and used results from the literature for other compounds, converged to similar accuracy. For these calculations we employed the QUANTUM ESPRESSO package [32] and the BERKELEYGW [33] code, to converge the conduction and valence band quasiparticle energies to within 5 meV; the results of these calculations and comparison to KS eigenvalues were discussed in detail by Shiang *et al.* [34].

III. STRUCTURE AND STABILITY

In Table I we collect the results on the structural features of the compounds studied here. The mixed compounds MXY have features that are very close to the average of the features of the two related pure compounds, MX_2 and MY_2 ($M =$ Mo, W and $X,Y =$ S, Se). In Fig. 1 we show the atomic structure and valence electron density of MoS_2, as a representative case of the compounds studied, at zero strain and at $\pm 3\%$ tensile/compressive strain. The application of strain slightly distorts the electronic density, resulting in $+1\%$ increase of the bond length $b_{M\text{-S}}$ for $+3\%$ tensile strain and -1% decrease of $b_{M\text{-S}}$ for -3% compressive strain. The two chalcogen atoms on either side of the central plane move farther apart from each other for compressive (negative) strain and closer to each other for tensile (positive) strain, thus partially mitigating the effect of lattice strain on the metal-chalcogen bond distances. The thickness d was chosen such that outside of this distance the charge density at a given point would be less than 10% of its maximal value. From the different lattice constants, we can infer that the free-standing mixed compounds MSSe would form a thin spherical shell, with the Se on the outer surface and the S on the inner surface, and with a radius of curvature $R = da/(a - a') \sim 15$ nm, for both the Mo and W based compounds, where a and a' are the lattice constants of the corresponding pure compounds $M\mathrm{Se}_2$ and $M\mathrm{S}_2$.

The cohesive energies in Table I were calculated using $E_{\text{coh}} = E - E_b(M) - 2E_b(X)$, where E is the total energy of the relevant MX_2 compound per unit formula, $E_b(M)$ is the total energy per atom for bulk M (taken as a BCC crystal) and $E_b(X)$ is the total energy per atom for bulk Se (modeled as helices with three atoms per unit cell) or bulk S (modeled as stacked S_8 rings). In the Se bulk structure, the bond length for nearest-neighbor atoms is 2.41 Å, the Se-Se-Se bond angle in a chain is 103.9°, and the minimum distance between chains is 3.53 Å. For the S bulk structure, we calculate the total energy of a gas phase S_8 molecule and then subtract the sublimation enthalpy [35] to obtain the total energy of the solid phase; in the molecule, the bond length is 2.06 Å, the average bond angle is 108.1°, and the average dihedral angle is 98.6°.

We obtain the in-plane stiffness of the TMDC monolayers from the expression [36]:

$$I = \frac{1}{A_0}\frac{\partial^2 E_s}{\partial \varepsilon^2}, \quad (1)$$

where A_0 is the equilibrium area of a unit cell of the monolayer and E_s is the difference between the total energy of the strained structure and the total energy of the system at equilibrium, expanded to second order in the components of the strain ε. The in-plane stiffness I is larger for shorter bonds ($I_{M\mathrm{S}_2} > I_{M\mathrm{SSe}} > I_{M\mathrm{Se}_2}$ for $M =$ Mo, W), consistent with previous results [25,37]; our value for the in-plane stiffness of MoS_2, 135.8 N/m, is well within the range of the experimental results, 180 ± 60 N/m [38]. W-based compounds are stiffer compared to Mo-based ones, since bonding orbitals are more extended in W than in Mo leading to greater overlap between metal and chalcogen orbitals and correspondingly stronger bonds.

TABLE I. Structural features of the pure MX_2 and mixed MXY TMDC compounds considered: lattice constant (a), distance along the plane-normal direction between metal and chalcogen layers ($d_{M\text{-S}}$, $d_{M\text{-Se}}$), bond lengths ($b_{M\text{-S}}$, $b_{M\text{-Se}}$), thickness (d) (all in Å), cohesive energies (E_{coh}) of equilibrium configurations (in eV), the in-plane stiffness I (in N/m), the dipole moment perpendicular to the plane of the 2D material, $p_\perp$, (in Debye, $D = 0.2082\ e$ Å), and the change in energy due to the presence of an Al-terminated polar AlN substrate, $\Delta E_{\text{b-pol}}$, (in eV). For the hybrid compounds, the changes in energy for the dipole oriented parallel (antiparallel) to the dipole of the substrate are indicated.

	a	$d_{M\text{-S}}$	$d_{M\text{-Se}}$	$b_{M\text{-S}}$	$b_{M\text{-Se}}$	d	E_{coh}	I	$p_\perp$	$\Delta E_{\text{b-pol}}$
MoS_2	3.18	1.56	—	2.41	—	6.15	−2.45	135.8	0	−0.79
MoSSe	3.24	1.53	1.71	2.42	2.53	6.30	−2.24	125.3	0.25	−0.89 (−0.56)
$MoSe_2$	3.32	—	1.67	—	2.54	6.45	−2.10	115.3	0	−0.64
WS_2	3.18	1.57	—	2.42	—	6.16	−2.26	151.4	0	−0.61
WSSe	3.25	1.53	1.71	2.42	2.54	6.32	−1.95	138.1	0.24	−0.72 (−0.40)
WSe_2	3.32	—	1.68	—	2.55	6.48	−1.71	127.4	0	−0.49

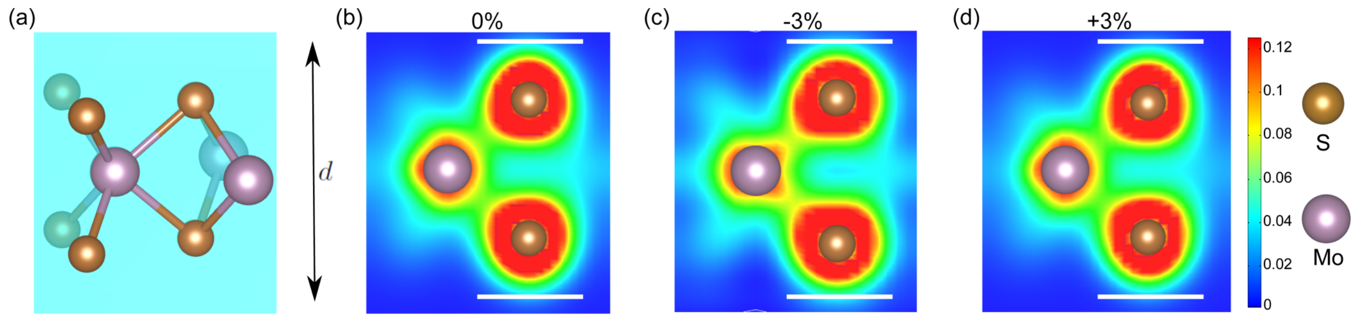

FIG. 1. (a) Atomic structure and (b)–(d) valence electron densities of MoS_2, a representative case of the compounds considered, for (b) zero strain, (c) −3% compressive strain, and (d) +3% tensile strain. The white lines in (b)–(d) indicate the boundaries that define the thickness d of the layer (see text for details).

For applications requiring materials with intrinsic dipole moment, the two mixed compounds, MoSSe and WSSe, are particularly interesting since they have a significant dipole perpendicular to the plane of about 0.24–0.25 D per MSSe unit, that is, ∼1/8 of the dipole moment of a water molecule. We calculate this dipole moment by integrating the product of the total charge density and the position vector over the unit cell, which gives unambiguous results for the component perpendicular to the slab whose charge density goes to zero at some value well within the dimension of the unit cell in this direction. We comment here on the possibility of creating such polar structures: This may be feasible by growth on polar substrates, like AlN, which exhibit strong polarity in the direction perpendicular to the surface. The value of the lattice constant for AlN is 3.11 Å [39], implying a lattice constant mismatch of about 4% between the substrate, which is wurtzite in bulk form, and the MSSe layer. The more stable termination for the AlN surface has Al on top [40,41]. We obtain a rough estimate of the dipole moment of such a surface from the bulk counterpart which gives values ranging from 0.99–1.53 D [42,43]. Growth by MBE methods may be well suited to promote the creation of these mixed compounds, since the atoms arriving on the surface will likely have a good chance of forming local structures with the proper orientation, influenced by the dipole moment of the substrate. The energies that would be gained with a polar AlN substrate are given in Table I. These energies were obtained by taking the difference between the energy of the attached MX_2/AlN or MXY/AlN structure and the energies of the isolated MX_2 or MXY and AlN structures. For the AlN slab, the surface closest to the TMDC is the Al-terminated one. We explored the six high-symmetry relative lateral shifts to determine the lowest energy configuration as well as the distance from the AlN slab to the TMDC layer for each structure. In Fig. 2, we show the calculated probability of formation of the mixed layers, using Boltzmann weights and the fractions f_M, f_{S}, and f_{Se} of reactant atoms, where $f_M = (u-1)f_{\mathrm{S}}$, $f_{\mathrm{Se}} = 1 - uf_{\mathrm{S}}$, with u some real number greater than 1, for the MX_2 and MXY systems (M = Mo, W), which are given by:

$$P^{(\pm)}_{M\mathrm{SSe}}(f_{\mathrm{S}}) = \frac{2f_{\mathrm{S}}f_{\mathrm{Se}}e^{-E^{(\pm)}_{M\mathrm{SSe}}/k_bT}}{f_{\mathrm{S}}^2e^{-E_{M\mathrm{S}_2}/k_bT} + 2f_{\mathrm{S}}f_{\mathrm{Se}}\left(e^{-E^{(+)}_{M\mathrm{SSe}}/k_bT} + e^{-E^{(-)}_{M\mathrm{SSe}}/k_bT}\right) + f_{\mathrm{Se}}^2e^{-E_{M\mathrm{Se}_2}/k_bT}}, \tag{2}$$

where the sign refers to the orientation of the dipole moment of MSSe relative to that of AlN (+ for parallel, − for antiparallel orientation). The energies in the Boltzmann factors are obtained by summing E_{coh} and $\Delta E_{\mathrm{b-pol}}$ from Table I. The lowest of these energies is that of the MS_2 compounds so, for a relatively high fraction of S atoms, formation of MS_2 is favored at ambient temperature. For higher temperature, the energy differences have less effect so a higher fraction of S atoms maximizes the probability of forming the mixed compounds. Naturally, a relatively large fraction of M atoms (u large) leads to a lower fraction of Se atoms maximizing the probability of forming the mixed compounds, which may be important for cost considerations, though if $f_M \gg f_{\mathrm{S}}$ more atoms would be wasted. Figure 3 shows the charge density difference, for MoSSe on AlN, calculated as $\Delta\rho = \rho_{\mathrm{MoSSe+AlN}} - \rho_{\mathrm{MoSSe}} - \rho_{\mathrm{AlN}}$. Due to the relative electronegativities of the atoms at the interface, charge accumulates in the region between the substrate and the adsorbate.

IV. ELECTRONIC PROPERTIES

We turn next our attention to the electronic properties of these systems. Since DFT underestimates the band gaps, we also use GW results from the literature as well as a self-consistent method for calculating excitonic effects to determine the values of optical and transport gaps that can be compared to experiment. To obtain the macroscopic dielectric function we use the reciprocal of the $\mathbf{G} = \mathbf{G}' = 0$ component of $\epsilon^{-1}_{\mathbf{GG}'}(\mathbf{q},\omega)$, the inverse of the microscopic dielectric matrix in reciprocal space, calculated within the random phase approximation [44]. This formulation ensures that local field effects are included.

To facilitate further discussion, we show in Fig. 4 the band structures of the mixed MoSSe and WSSe compounds, which have not been previously considered. These resemble closely the band structures of the pure compounds, MS_2 and MSe_2 (M = Mo, W), with relatively minor differences. By projecting out the contributions of the atomic orbitals of

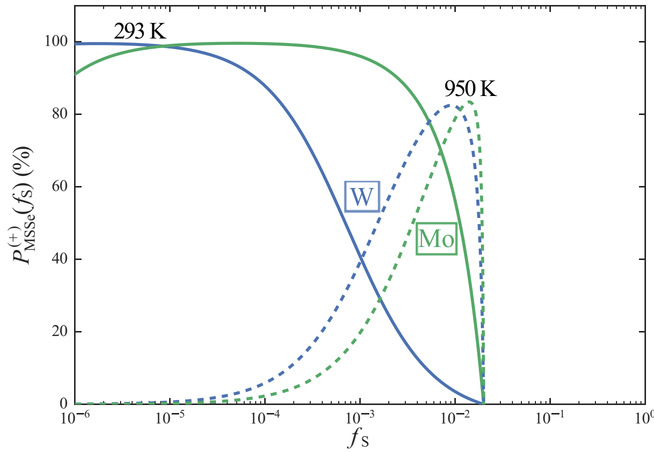

FIG. 2. Probability $[P^{(+)}_{MSSe}(f_S)]$, Eq. (2), of producing the MSSe mixed compounds (M = Mo, green curves or M = W, blue curves) with dipole moment oriented parallel to the dipole moment of an AlN substrate as a function of the fraction of S atoms in the source, for two different values of temperature, $T = 293$ K and $T = 950$ K. The probability for antiparallel polarization $[P^{(-)}_{MSSe}(f_S)]$ is negligibly small and not shown here; this is expected on physical grounds (parallel polarization is strongly favored since it minimizes the electrostatic energy at the interface). For the plot, we have taken $u = 50$.

different atoms to the wave functions, we confirm that the states of the valence and conduction band extrema near high symmetry points mainly originate from the $3p(4p)$ orbitals of the S (Se) atoms and the $4d(5d)$ orbitals of Mo (W) atoms, as in the pure compounds [15,34]. Variation in strain changes the hybridization of these orbitals, and hence shifts the energies of the relevant states, as discussed next.

Bulk TMDCs are indirect band-gap semiconductors. However, monolayers of TMDCs exhibit direct band gaps [22], though these are sensitive to in-plane strain (see Fig. 5). The range of strain considered here was chosen to illustrate trends; typically accessible strains are probably confined to smaller values, though for MoS_2 breaking only occurs at an effective strain of 6 to 11% [38]. Under a compressive or tensile isotropic strain, each material in monolayer form makes a transition to an indirect band-gap semiconductor and the gap decreases both with compressive and tensile strain. Spin-orbit coupling (SOC) effects play a significant role in determining the value of the band gap, as shown in Fig. 5, where results with and without SOC corrections are presented for comparison. Our calculations indicate that WSe_2 is the least sensitive to strain (exhibiting robustness of the direct band gap), whereas the lighter compounds MoS_2 and MoSSe are the most sensitive. Between the K and Q points there are two contributions from SOC that conspire to decrease the gap, one from the conduction band at the Q point and one from the valence band at the K point. For the direct gap at the K point there is only one contribution from the valence band, and for the transition between the Γ and the K point there is negligible contribution, due in part to Kramers degeneracy. Thus, compounds with large SOC interaction exhibit a downward shift of the indirect $K \rightarrow Q$ gap value (red line in Fig. 5) when these contributions are included. A similar shift is found for the direct $K \rightarrow K$ gap (black line in Fig. 5), to a lesser extent, while this effect is absent in the results for the indirect $\Gamma \rightarrow$ K gap (green line in Fig. 5). The result is that for the heavier compounds the direct band gap region will be extended to larger strains. This

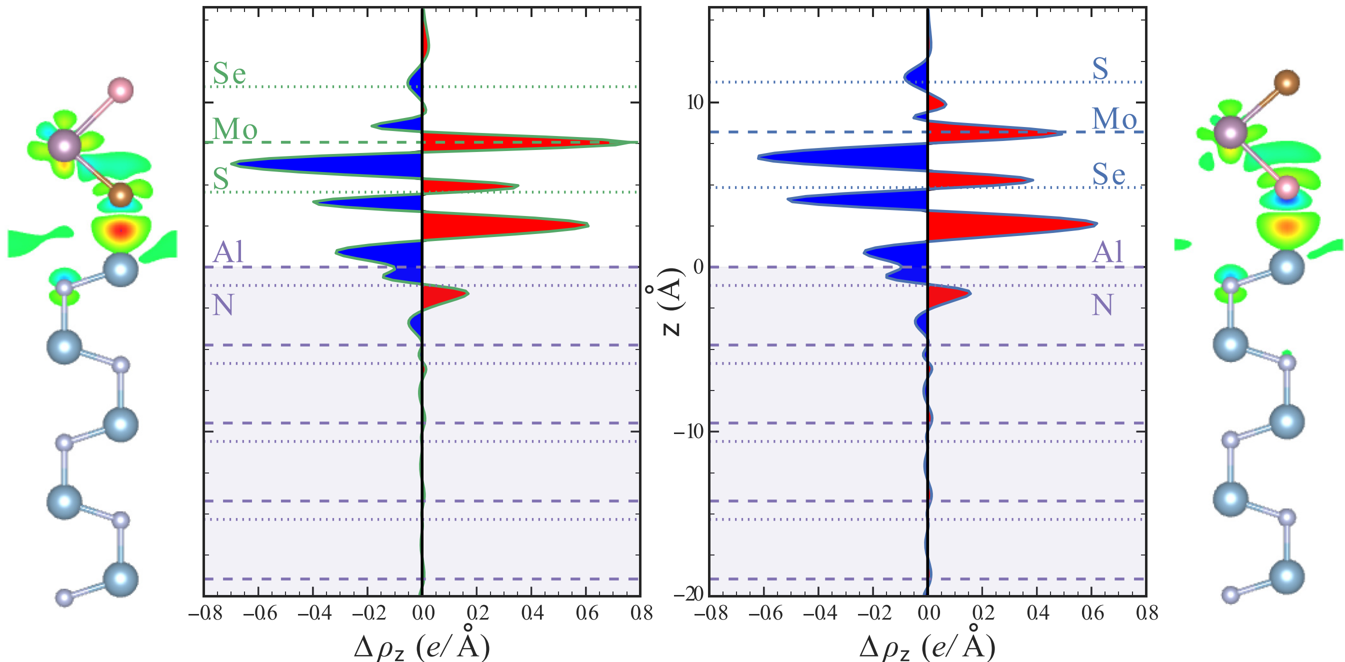

FIG. 3. The charge density difference between the combined MoSSe-AlN system and the sum of the isolated MoSSe and AlN substrate and the plane-averaged electron density difference ($\Delta\rho_z$) along the direction perpendicular to the interface of MoSSe-AlN with the dipole moment of the MoSSe oriented parallel and antiparallel to the dipole moment of the substrate; red indicates charge accumulation and blue charge depletion.

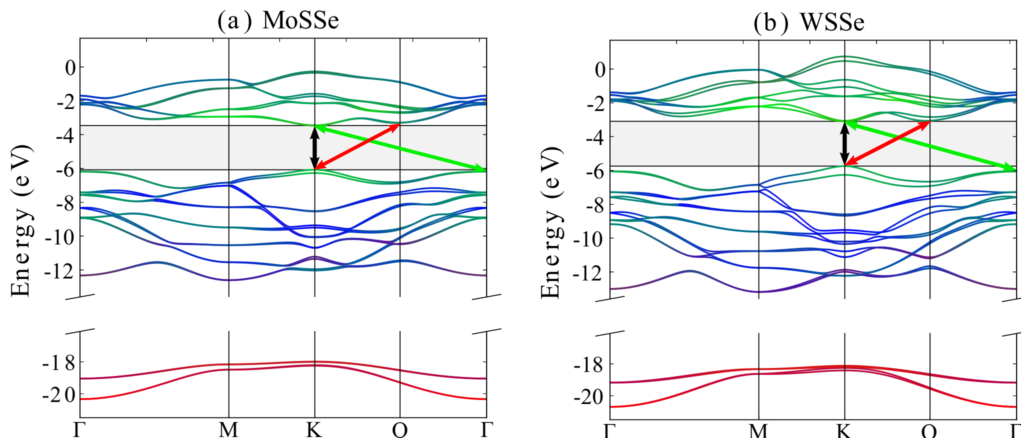

FIG. 4. Band structure plots for (a) MoSSe and (b) WSSe at zero strain; DFT values were rescaled according to our GW calculations and those of Ramasubramaniam [45], with bands color-coded to denote their orbital character: red = s, blue = p, green = d; these results include spin-orbit coupling (SOC). The double-headed black, red, and green arrows indicate pairs of states that define the direct or indirect band gaps, depending on the strain; at zero strain, the band is direct (black arrow) at K.

is due to the fact that the spin-orbit interaction will shrink the direct band gap, though not the $\Gamma \rightarrow K$ gap, and therefore it will shift the crossing point of the direct band gap and the indirect $\Gamma \rightarrow K$ gap curves towards larger positive strains. The compounds with the largest effects of this type are $MoSe_2$, WSSe, and WSe_2, as indicated explicitly by the downward arrows in Fig. 5.

We investigate next the effect of strain on the component of the dielectric function parallel to the plane of the layer, $\epsilon_{\parallel}(\omega)$. This effect of strain on the dielectric function is important because dielectric screening of the MoS_2 monolayer enhances mobility [7] and affects excitonic binding energies, thus influences the photoluminescence [46]. Knowledge of the dielectric function is therefore of particular importance in heterostructures consisting of multiple layers of TMDCs. Generally, the dielectric screening is optimal when $\mathrm{Im}[\epsilon_{\parallel}(\omega)]/\mathrm{Re}[\epsilon_{\parallel}(\omega)]$ is near zero, which implies that losses are minimal. In order to obtain values of the dielectric function that are independent of the size of the periodic cell which contains both the monolayer and the vacuum region, we need to transform the real calculated values to $\mathrm{Re}[\epsilon_{\parallel}(\omega)]$, where

$$\mathrm{Re}[\epsilon_{\parallel}(\omega)] = (\mathrm{Re}[\epsilon_{\parallel}^{\mathrm{DFT}}(\omega)] - 1)c/d + 1 \tag{3}$$

with c being the total length of the periodic unit cell in the z direction and d the thickness of a single layer as defined in Fig. 1 and tabulated in Table I. This scaling gives accurate values of the dielectric constant and is obtained by using the rules for addition of capacitance in series and in parallel in agreement with results found in literature [47]. A similar expression applies to the dielectric function component perpendicular to the layer, specifically to $\mathrm{Re}[\epsilon_{\perp}^{\mathrm{DFT}}(\omega)]^{-1}$, and the imaginary part of the dielectric function is rescaled by the factor c/d.

We find that the dielectric constant or relative permittivity tends to increase with strain and can thus be used as a signature to measure the strain in these compounds. We discuss as representative examples the dielectric functions of MoS_2 and WSe_2, which show similar behavior, as do all the other compounds we considered. The features labeled X_1 and X_2 in the plots of $\mathrm{Re}[\epsilon_{\parallel}(\omega)]$ in Fig. 6 originate from the direct transition at the K point; from Fig. 5 we see that these features track closely with the direct band gap as a function of strain. The larger-amplitude and more diffuse feature at ω between 2 and 3 eV traces its origin in the regions near the Q and Γ points. With tensile strain (increase in the lattice constant), the peaks in the absorption spectrum or imaginary part of $\epsilon_{\parallel}(\omega)$, which correspond to interband excitations, shift to lower energy (see Fig. 6).

We next turn our attention to obtaining values of the band gaps that can be directly compared to experimental measurements. It is well established that band gap values obtained from DFT are underestimates of those measured in experiment. There are two main reasons for this discrepancy: (i) differences in single-particle energies of the Kohn-Sham equations, which are used to obtain the DFT band gaps, are physically justifiable for the ground state but not for excited states that involve moving an electron from a valence to a conduction band across the band gap, and (ii) there is a derivative discontinuity in the exact exchange-correlation energy at integer particle numbers [54]. To address the first issue, the correct excitation energies can be calculated by solving for the quasiparticle energies from the self-energy operator [55,56]; though this is a useful and highly accurate approach as implemented by the GW approximation, the computations are quite expensive. To address the second issue, various formulas for correcting the derivative discontinuity have been derived, that give reasonable results for 3D solids. We have attempted to apply one of these corrections [57] but found that they do not give satisfactory results for the TMDC single layers considered here. We show in Fig. 7 the values obtained from GW calculations and compare them to values obtained from transport measurements, which are quite large (in the range of 2.4–2.8 eV); there is quite reasonable agreement between the GW results for all the compounds considered here. By contrast, the results from DFT calculations, that is, the difference between the valence band maximum and conduction band minimum of Kohn-Sham eigenvalues (in the range 1.3–1.6 eV) is a very significant underestimate of the

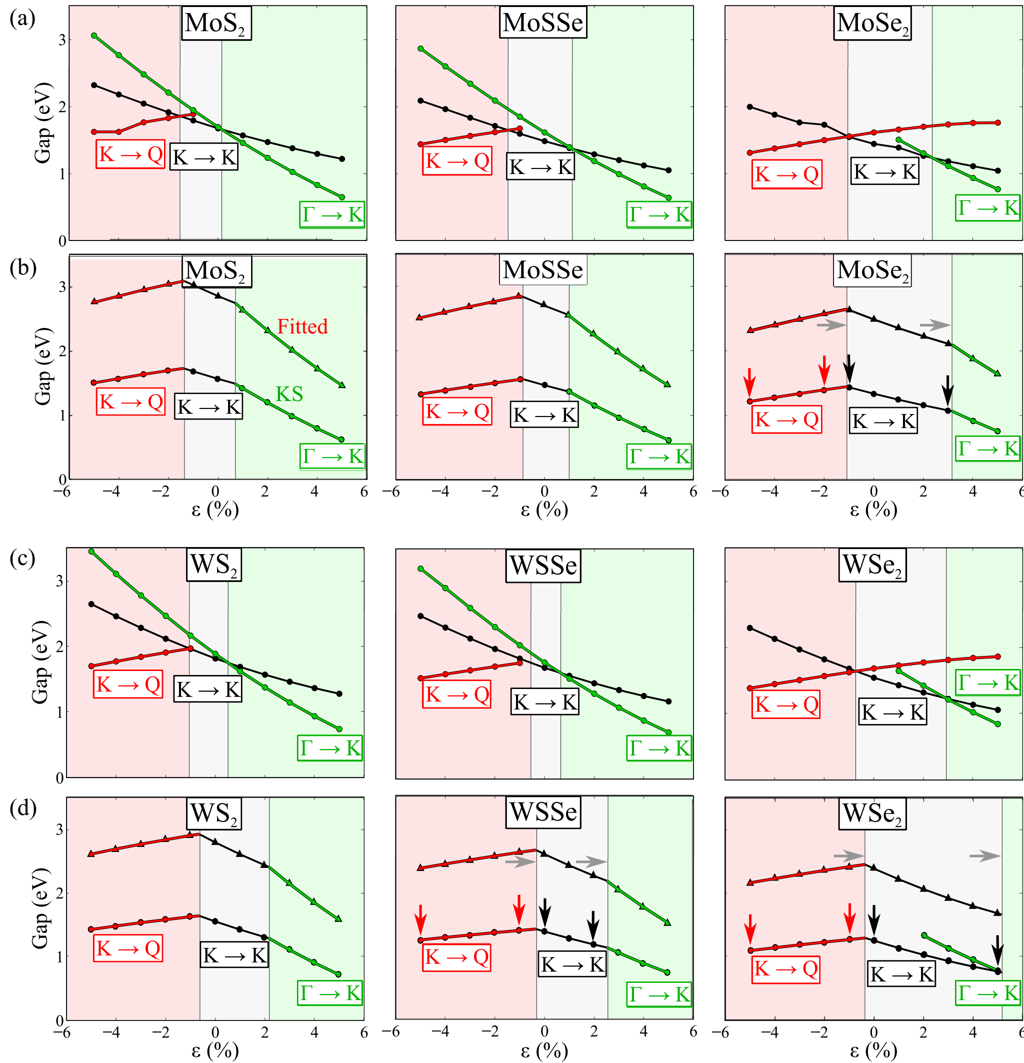

FIG. 5. Phase diagrams showing the transition from a direct to an indirect band-gap semiconductor for: (a) and (b) Mo-based structures and (c) and (d) W-based structures; for comparison we show results both without [(a) and (c)] and with [(b) and (d)] SOC effects in each case. The transitions indicate lowest band gaps, indirect (K → Q, red or Γ → K, green) and direct (K → K, black); color shaded regions identify the corresponding indirect gap ranges depending on strain. Downward (black and red) and side (gray) arrows indicate the most significant changes introduced by the inclusion of SOC effects. The upper curves (triangles) in [(b) and (d)] are adjusted values to match GW gaps at zero strain and assuming the same strain dependence as in the KS gaps (see text for details).

experimental band gaps, by approximately 50%, as is typical. In order to reconcile the Kohn-Sham eigenvalues with the GW results, we adjust the KS values by the amount they differ from the GW result at zero strain and assume the same strain dependence; the results are shown in Fig. 5, and can be taken as an approximation to the true transport gap as a function of strain. The optical gap can then be obtained from the exciton binding energies presented in Sec. V. The GW corrections can be state dependent and might therefore affect the direct and indirect band gaps differently, which will affect the direct-gap windows shown in Fig. 5; however, the overall trends, as dictated by the influence of SOC, should still hold.

V. EXCITONIC EFFECTS

The results discussed so far, both experiment and theory, do not include excitonic effects, as is appropriate for transport measurements. To account for excitonic effects, we investigate the binding of excitons at K valleys, corresponding to the zero strain case and a direct band gap for all the materials investigated, within the effective mass approximation, using a classical interaction potential between electron and hole charges [58,59]. We adopt a model for the TMDC layer consisting of a quasi-two-dimensional anisotropic dielectric slab of thickness d with the in-plane (out-of-plane) dielectric constant $\epsilon_{\parallel}$ ($\epsilon_{\perp}$) immersed in vacuum, or including a substrate. We use two different models to calculate the exciton binding energies, one in which the electron and the hole are treated as lines that span the thickness of the layer and one in which they are treated as point particles, as shown in the schematic diagrams in Fig. 7. The first model [60] takes into consideration the fact that the electron and the hole are described by wave functions that are likely to be nonzero through the entire thickness of the layer. The results of this model agree with

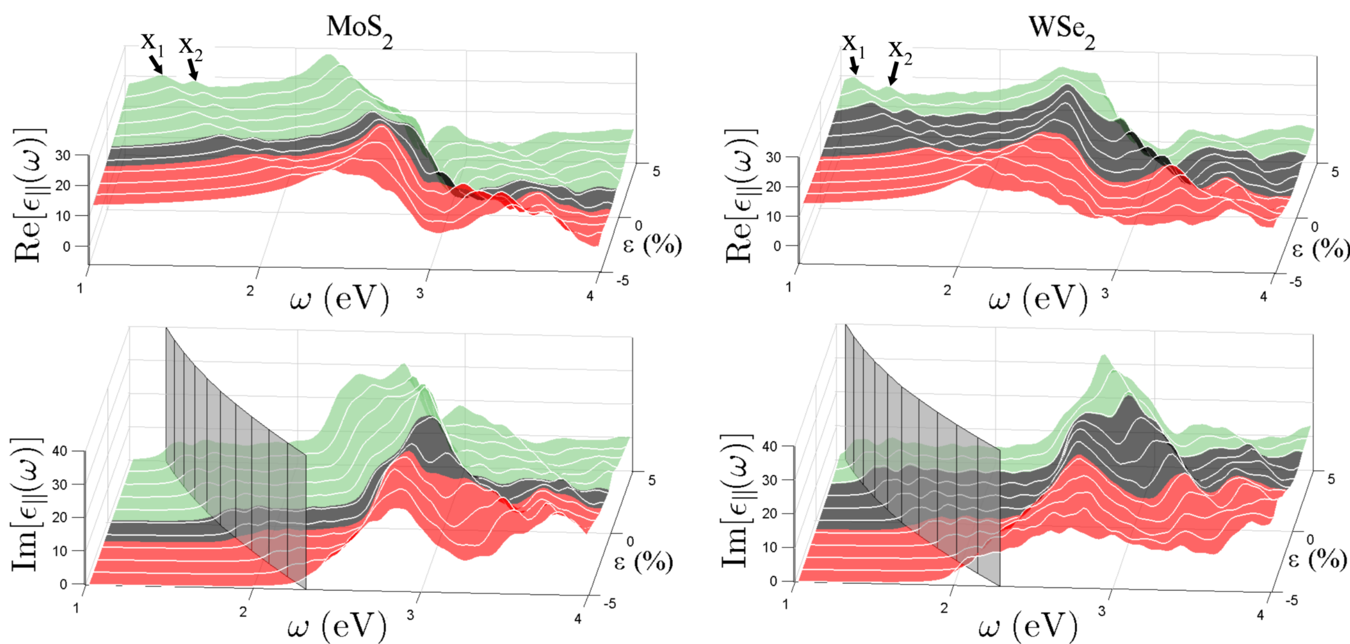

FIG. 6. Real and imaginary parts of the dielectric function, Re[$\epsilon_{\parallel}(\omega)$], Im[$\epsilon_{\parallel}(\omega)$], for MoS_2 and WSe_2 for in-plane strain ranging from −5% to +5% in increments of 1%. The color coding reflects the nature of the band gap that corresponds to each strain value, with the same conventions as in Fig. 5. The minimum direct band gaps, which signal the onset of absorption, are identified by the gray surface in the plots for the imaginary part of the dielectric function. The dielectric function has been transformed to $\epsilon_{\parallel}(\omega)$ from Eq. (3), see text.

the strict 2D limit model often given in the literature [61]. The second model, the limit of the two charges being point particles, is also a sensible approach since the electron and hole wave functions are mainly composed of the relatively localized metal d orbitals as we have shown recently [34]. The Poisson equation for the electrostatic problem can be analytically solved with the help of a partial Fourier transformation for the in-plane xy coordinate [59,62]. The potential between two

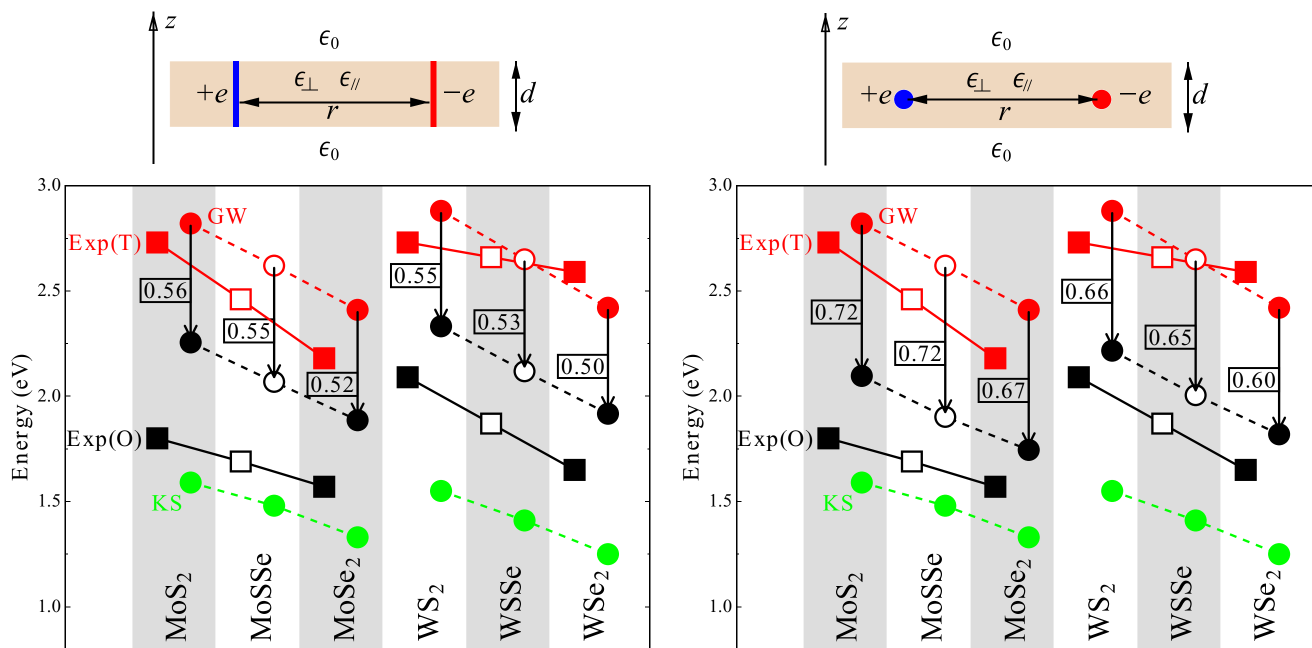

FIG. 7. Band gaps from theory without excitonic effects, KS (green circles) and GW [45] (red circles) compared to experimental transport measurements [46,48–50] (red squares), and from theory with excitonic effects (shifted black circles) obtained with the line (left panel) or point (right panel) charge models, compared to experimental optical measurements [51–53] (black squares). The arrows and corresponding numbers indicate the calculated exciton binding energies from each model. Open squares and circles indicate that the values were calculated as the average of the corresponding MS_2 and MSe_2 gaps.

charges $\pm e$ in a layer of thickness d is given by:

$$U(r) = \frac{-e^2}{4\pi\epsilon_0\lambda}\int_0^\infty J_0(qr)K(q)dq, \quad (4)$$

where the kernel $K(q)$ takes different forms: for the two line charges

$$K_{\text{line}}(q) = \left[1 - \frac{1}{(\kappa qd/2)[\lambda + \coth(\kappa qd/2)]}\right]\frac{1}{(\kappa qd/2)} \quad (5)$$

whereas for two point charges

$$K_{\text{point}}(q) = \left[\frac{\lambda + \tanh(\kappa qd/2)}{1 + \lambda\tanh(\kappa qd/2)}\right], \quad (6)$$

where $q = |\vec{q}|$ for the two-dimensional in-plane momentum and J_0 is the Bessel function of the first kind and we have defined $\lambda = (\epsilon_\parallel\epsilon_\perp)^{1/2}$ and $\kappa = (\epsilon_\parallel/\epsilon_\perp)^{1/2}$. With this potential, we can then solve numerically the effective mass Schrödinger equation in the relative coordinate of the electron and the hole charged particle, using a logarithmic grid. All values that enter in these equations, including the dielectric constants $\epsilon_\parallel,\epsilon_\perp$, and the effective masses for the electron and hole, are obtained from the first-principles calculations described earlier, so the results do not involve any adjustable parameters. The results from both models are shown in Fig. 7. The inclusion of excitonic effects with the line-charge model produces values for the optical gaps that are on average 0.54 eV lower than the transport gaps, but this is still far from the corresponding experimental values. In contrast to this, the results from the point-charge model are in better agreement with the optical gaps from experiment, and involve an average binding energy of the excitons of ~0.64 eV for the W compounds and ~0.70 eV for the Mo compounds. From this comparison, it appears that the point-charge model is closer to the physical picture of how excitons behave in these layered compounds. We have also explored the effect of a substrate, using the kernel:

$$K_{\text{pt-s}}(q) = 2\left[\frac{(\lambda\cosh(\kappa qd/2) + \sinh(\kappa qd/2))(\lambda\cosh(\kappa qd/2) + \epsilon_s\sinh(\kappa qd/2))}{(1+\epsilon_s)\lambda\cosh(\kappa qd) + (\epsilon_s + \lambda^2)\sinh(\kappa qd)}\right], \quad (7)$$

where ϵ_s is the relative permittivity of the substrate. We investigate the dependence of the binding energy of the exciton on the relative permittivity of the substrate in Fig. 8 for the monolayer MoS_2 and WS_2 systems for which accurate measurements of the exciton binding energy exist. The results of Fig. 8 indicate the possible effective values of the relative permittivity of the substrate that could explain the observed binding energies. These effective values could be the result of combining the relative permittivity of the pure substrates (Si, SiO_2, h-BN) in a way that reflects the actual composition and structure of the substrate, about which there is not enough quantitative information to allow us a more precise estimate. Additional effects due to charge accumulation at the interface in the presence of a polar substrate may also come into play. The transport gap will also be reduced as a result of the polarization-induced screening effect of the substrate. Indeed, a reduction in the GW band gap of carbon nanotubes of 0.35 eV is observed when they are deposited on h-BN [63]. This suggests the optical gap would remain relatively unchanged, but detailed calculations are necessary to determine the magnitude of this effect.

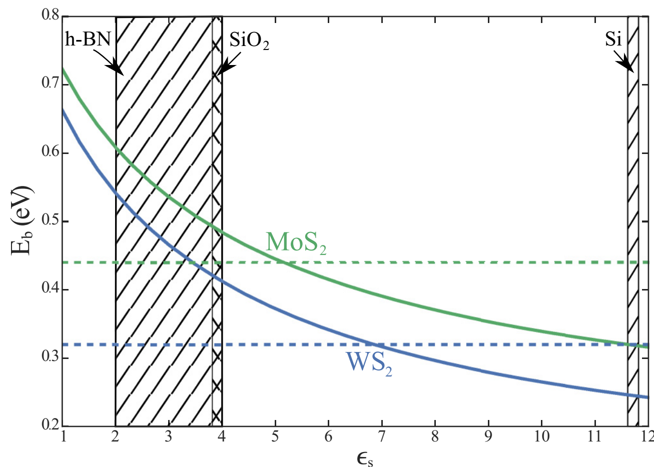

FIG. 8. Binding energy of the exciton as a function of relative permittivity of the substrate ϵ_s. The horizontal dashed lines indicate experimental measurements of the binding energy [53,64]. The measurements on monolayer WS_2 were done on a SiO_2/Si substrate, while those on monolayer MoS_2 were done on a flake of h-BN on SiO_2/Si. The relative permittivity of SiO_2 is ~3.9 [65], of Si is ~11.7, and of h-BN is in the range 2 to 4 [66]; these relative permittivity values are indicated by the shaded regions.

The key parameters that enter in the determination of the exciton binding energies are the dielectric constant ($\epsilon_\parallel,\epsilon_\perp$) and the reduced mass of the electron-hole pair μ, both of which can be changed by applying strain. To investigate this, we show in Fig. 9 the values of these quantities for various materials as functions of strain and the resulting binding energies of the excitons in the lowest-energy state corresponding to zero angular momentum, as obtained from the point-charge model. The out-of-plane dielectric constant $\epsilon_\perp$ is affected less and varies almost linearly with strain, with values of 4.0 to 3.2 for MoS_2 and WS_2, 4.4 to 3.4 for MoSSe and WSSe, and 4.9 to 3.7 for $MoSe_2$ and WSe_2 for strain in the −5% to +5% range. The in-plane dielectric constant $\epsilon_\parallel$ shows stronger dependence on strain and on the composition of the compound, as shown in Fig. 9(a). The variation of the reduced exciton mass μ with strain is mild and is most pronounced for the mixed compounds MXY. The resulting variation in exciton binding energies is monotonic and almost linear with strain for the pure compounds and somewhat stronger for the mixed compounds, with nonlinear behavior (stronger dependence) for compressive strain.

VI. CONCLUSION

In this paper we explored the effect of strain and composition on the structural, electronic, and optical properties

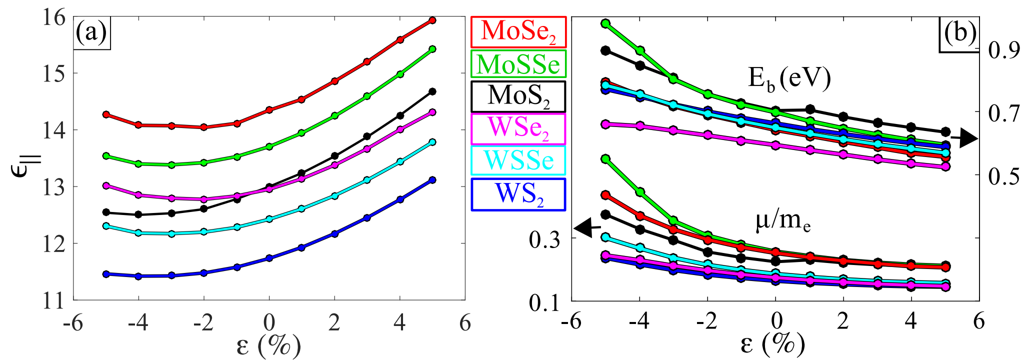

FIG. 9. (a) Dielectric constant values in the plane ($\epsilon_{\parallel}$) of the monolayers MoS_2, MoSSe, $MoSe_2$, WS_2, WSSe, and WSe_2. (b) Effective masses (μ) in units of the bare electron mass and exciton binding energies (E_b) obtained by approximating the electron and hole as point charges.

of MXY TMDC materials, with $M =$ Mo, W and $X,Y =$ S, Se. We find that, at the level of GW calculations, the band gaps obtained from theory are in reasonable agreement with band gaps from transport measurements and are in the range 2.4–2.8 eV. The band gaps are sensitive to applied strain and can change from direct to indirect, for both compressive and tensile strain; the indirect gaps induced by strain are different for different signs of the strain: They occur between the K and Q points of the BZ for negative (compressive) strain and between the Γ and K points for positive (tensile) strain. Though the choice ultimately depends on the application, WSe_2 is a good candidate material for optoelectronics since the direct gap is preserved for a wide range of tensile in-plane strain. A tensile in-plane strain is induced in most epitaxial MX_2 materials during cooling from the growth temperature down to room temperature because these materials typically have a larger thermal expansion coefficient than conventional substrates, therefore, during cooling, the MX_2 in order to comply with the substrate lattice becomes stretched. The strain also affects optical properties, as evidenced by a shift in peaks of the dielectric function with applied strain.

In order to make quantitative comparisons with optically measured gaps, we include excitonic effects within the effective mass approximation using a screened interaction potential between electrons and holes, which are modeled in the two physically plausible limits as either line or point charges within each layer. For our point charge model, the exciton corrections yield band gaps which are in good agreement with optically measured values. We also analyze substrate effects on the exciton binding energies since the presence of the substrate introduces an effective relative permittivity, which can be obtained by taking into consideration the substrate composition and structure. The effective permittivity of the substrate has a significant effect on the exciton binding energy and brings the calculated values well within range of experimentally measured ones.

Overall, we find that the use of strain and composition as independent parameters for tuning the material properties can be very effective: For example, in the case of the mixed MoXY compound, compressive strain of -5% can lead to exciton binding energies in excess of 0.9 eV. The information from our calculations makes it feasible to identify the material with the desired value of the band gap over a range which is considerably extended over the inherent values in strain-free layers. Specifically, the band-gap range for the pure and mixed compounds we considered can be from 1.5 to 3.1 eV for the transport gap and from 1.0 to 2.1 eV for the optical gap, by the proper combination of strain, compound composition, and substrate choice.

ACKNOWLEDGMENTS

We thank Dmitry Vinichenko and Wei Chen for useful discussions. We acknowledge support by ARO MURI Grant No. W911NF-14-1-0247 (S.N.S., G.A.T., and E.K.) and by the STC Center for Integrated Quantum Materials, NSF Grant No. DMR-1231319 (S.F.).

[1] G. Xu, J. Wang, B. Yan, and X.-L. Qi, Topological superconductivity at the edge of transition-metal dichalcogenides, Phys. Rev. B **90**, 100505 (2014).

[2] T. Ritschel, J. Trinckauf, K. Koepernik, B. Buchner, M. v. Zimmermann, H. Berger, Y. I. Joe, P. Abbamonte, and J. Geck, Orbital textures and charge density waves in transition metal dichalcogenides, Nat. Phys. **11**, 328 (2015).

[3] C. Drummond, N. Alcantar, J. Israelachvili, R. Tenne, and Y. Golan, Microtribology and friction-induced material transfer in WS_2 nanoparticle additives, Adv. Funct. Mater. **11**, 348 (2001).

[4] L. Byskov, J. Nørskov, B. Clausen, and H. Topsøe, Edge termination of MoS_2 and CoMoS catalyst particles, Catal. Lett. **64**, 95 (2000).

[5] W. Sienicki and T. Hryniewicz, Tungsten diselenide heterojunction photoelectrodes, Sol. Energy Mater. Sol. Cells **43**, 67 (1996).

[6] A. Kuc, N. Zibouche, and T. Heine, Influence of quantum confinement on the electronic structure of the transition metal sulfide TS_2, Phys. Rev. B **83**, 245213 (2011).

[7] B. Radisavljevic, A. Radenovic, J. Brivio, V. Giacometti, and A. Kis, Single-layer MoS_2 transistors, Nat. Nano **6**, 147 (2011).

[8] W. Zhang, C.-P. Chuu, J.-K. Huang, C.-H. Chen, M.-L. Tsai, Y.-H. Chang, C.-T. Liang, Y.-Z. Chen, Y.-L. Chueh, J.-H. He, M.-Y. Chou, and L.-J. Li, Ultrahigh-gain photodetectors based on atomically thin graphene-MoS_2 heterostructures, Sci. Rep. **4**, 3826 (2014).

[9] S. Bertolazzi, D. Krasnozhon, and A. Kis, Nonvolatile memory cells based on MoS_2/graphene heterostructures, ACS Nano **7**, 3246 (2013).

[10] F. Withers, O. Del Pozo-Zamudio, A. Mishchenko, A. P. Rooney, A. Gholinia, K. Watanabe, T. Taniguchi, S. J. Haigh, A. K. Geim, A. I. Tartakovskii, and K. S. Novoselov, Light-emitting diodes by band-structure engineering in van der waals heterostructures, Nat. Mater. **14**, 301 (2015).

[11] K. E. Aretouli, P. Tsipas, D. Tsoutsou, J. Marquez-Velasco, E. Xenogiannopoulou, S. A. Giamini, E. Vassalou, N. Kelaidis, and A. Dimoulas, Two-dimensional semiconductor $HfSe_2$ and $MoSe_2/HfSe_2$ van der Waals heterostructures by molecular beam epitaxy, Appl. Phys. Lett. **106**, 143105 (2015).

[12] E. Xenogiannopoulou, P. Tsipas, K. E. Aretouli, D. Tsoutsou, S. A. Giamini, C. Bazioti, G. P. Dimitrakopulos, P. Komninou, S. Brems, C. Huyghebaert, I. P. Radu, and A. Dimoulas, High-quality, large-area $MoSe_2$ and $MoSe_2/Bi_2Se_3$ heterostructures on AlN(0001)/Si(111) substrates by molecular beam epitaxy, Nanoscale **7**, 7896 (2015).

[13] W. S. Yun, S. W. Han, S. C. Hong, I. G. Kim, and J. D. Lee, Thickness and strain effects on electronic structures of transition metal dichalcogenides: 2H-MX_2 semiconductors (M = Mo, W; X = S, Se, Te), Phys. Rev. B **85**, 033305 (2012).

[14] H. J. Conley, B. Wang, J. I. Ziegler, R. F. Haglund, S. T. Pantelides, and K. I. Bolotin, Bandgap engineering of strained monolayer and bilayer MoS_2, Nano Lett. **13**, 3626 (2013).

[15] E. Scalise, M. Houssa, G. Pourtois, V. Afanas'ev, and A. Stesmans, Strain-Induced Semiconductor to Metal Transition in the Two-Dimesional Honeycomb Structure of MoS_2, Nano Res. **5**, 43 (2011).

[16] Q. Zhang, Y. Cheng, L.-Y. Gan, and U. Schwingenschlögl, Giant valley drifts in uniaxially strained monolayer MoS_2, Phys. Rev. B **88**, 245447 (2013).

[17] H. Rostami, R. Roldán, E. Cappelluti, R. Asgari, and F. Guinea, Theory of strain in single-layer transition metal dichalcogenides, Phys. Rev. B **92**, 195402 (2015).

[18] P.-C. Yeh, W. Jin, N. Zaki, J. Kunstmann, D. Chenet, G. Arefe, J. T. Sadowski, J. I. Dadap, P. Sutter, J. Hone, and J. Richard M. Osgood, Direct Measurement of the Tunable Electronic Structure of Bilayer MoS_2 by Interlayer Twist, Nano Lett. **16**, 953 (2016).

[19] W. Jin, P.-C. Yeh, N. Zaki, D. Zhang, J. T. Liou, J. T. Sadowski, A. Barinov, M. Yablonskikh, J. I. Dadap, P. Sutter, I. P. Herman, and R. M. Osgood, Substrate interactions with suspended and supported monolayer MoS_2: Angle-resolved photoemission spectroscopy, Phys. Rev. B **91**, 121409 (2015).

[20] P.-C. Yeh, W. Jin, N. Zaki, D. Zhang, J. T. Liou, J. T. Sadowski, A. Al-Mahboob, J. I. Dadap, I. P. Herman, P. Sutter, and R. M. Osgood, Layer-dependent electronic structure of an atomically heavy two-dimensional dichalcogenide, Phys. Rev. B **91**, 041407 (2015).

[21] K.-A. N. Duerloo and E. J. Reed, Structural phase transitions by design in monolayer alloys, ACS Nano **10**, 289 (2016).

[22] Q. H. Wang, K. Kalantar-Zadeh, K. Andras, J. N. Coleman, and M. S. Strano, Electronics and optoelectronics of two-dimensional transition metal dichalcogenides, Nat. Nanotechnol. **7**, 699 (2012).

[23] J. A. Wilson and A. D. Yoffe, The transition metal dichalcogenides discussion and interpretation of the observed optical, electrical and structural properties, Adv. Phys. **18**, 193 (1969).

[24] K.-A. N. Duerloo, M. T. Ong, and E. J. Reed, Intrinsic piezoelectricity in two-dimensional materials, J. Phys. Chem. Lett. **3**, 2871 (2012).

[25] D. M. Guzman and A. Strachan, Role of strain on electronic and mechanical response of semiconducting transition-metal dichalcogenide monolayers: An *ab-initio* study, J. Appl. Phys. **115**, 243701 (2014).

[26] L. Wang, A. Kutana, and B. I. Yakobson, Many-body and spin-orbit effects on direct-indirect band gap transition of strained monolayer MoS_2 and WS_2, Ann. Phys. **526**, L7 (2014).

[27] J. J. Mortensen, L. B. Hansen, and K. W. Jacobsen, Real-space grid implementation of the projector augmented wave method, Phys. Rev. B **71**, 035109 (2005).

[28] J. Enkovaara, C. Rostgaard, J. J. Mortensen, J. Chen, M. Dułak, L. Ferrighi, J. Gavnholt, C. Glinsvad, V. Haikola, H. A. Hansen, H. H. Kristoffersen, M. Kuisma, A. H. Larsen, L. Lehtovaara, M. Ljungberg, O. Lopez-Acevedo, P. G. Moses, J. Ojanen, T. Olsen, V. Petzold, N. A. Romero, J. Stausholm-Møller, M. Strange, G. A. Tritsaris, M. Vanin, M. Walter, B. Hammer, H. Häkkinen, G. K. H. Madsen, R. M. Nieminen, J. K. Nørskov, M. Puska, T. T. Rantala, J. Schiøtz, K. S. Thygesen, and K. W. Jacobsen, Electronic structure calculations with gpaw: A real-space implementation of the projector augmented-wave method, J. Phys.: Condens. Matter **22**, 253202 (2010).

[29] S. R. Bahn and K. W. Jacobsen, An object-oriented scripting interface to a legacy electronic structure code, Comput. Sci. Eng. **4**, 56 (2002).

[30] P. E. Blöchl, Projector augmented-wave method, Phys. Rev. B **50**, 17953 (1994).

[31] J. P. Perdew, K. Burke, and M. Ernzerhof, Generalized Gradient Approximation Made Simple, Phys. Rev. Lett. **77**, 3865 (1996).

[32] P. Giannozzi, S. Baroni, N. Bonini, M. Calandra, R. Car, C. Cavazzoni, D. Ceresoli, G. L. Chiarotti, M. Cococcioni, I. Dabo, A. D. Corso, S. de Gironcoli, S. Fabris, G. Fratesi, R. Gebauer, U. Gerstmann, C. Gougoussis, A. Kokalj, M. Lazzeri, L. Martin-Samos, N. Marzari, F. Mauri, R. Mazzarello, S. Paolini, A. Pasquarello, L. Paulatto, C. Sbraccia, S. Scandolo, G. Sclauzero, A. P. Seitsonen, A. Smogunov, P. Umari, and R. M. Wentzcovitch, QUANTUM ESPRESSO: A modular and open-source software project for quantum simulations of materials, J. Phys.: Condens. Matter **21**, 395502 (2009).

[33] J. Deslippe, G. Samsonidze, D. A. Strubbe, M. Jain, M. L. Cohen, and S. G. Louie, BerkeleyGW: A massively parallel computer package for the calculation of the quasiparticle and optical properties of materials and nanostructures, Comp. Phys. Commun. **183**, 1269 (2012).

[34] S. Fang, R. Kuate Defo, S. N. Shirodkar, S. Lieu, G. A. Tritsaris, and E. Kaxiras, *Ab initio* tight-binding hamiltonian for transition metal dichalcogenides, Phys. Rev. B **92**, 205108 (2015).

[35] R. Steudel, *Elemental Sulfur and Sulfur-Rich Compounds I* (Springer, Heidelberg, 2003).

[36] M. Topsakal, S. Cahangirov, and S. Ciraci, The response of mechanical and electronic properties of graphane to the elastic strain, Appl. Phys. Lett. **96**, 091912 (2010).

[37] J. Kang, S. Tongay, J. Zhou, J. Li, and J. Wu, Band offsets and heterostructures of two-dimensional semiconductors, Appl. Phys. Lett. **102**, 012111 (2013).

[38] S. Bertolazzi, J. Brivio, and A. Kis, Stretching and breaking of ultrathin MoS_2, ACS Nano **5**, 9703 (2011).

[39] O. Madelung, *Semiconductors: Data Handbook*, 3rd ed. (Springer, Berlin, 2004).

[40] D. Holec and P. H. Mayrhofer, Reconstructions of the AlN(0001) surface, Scripta Mater. **67**, 760 (2012).

[41] C. D. Lee, Y. Dong, R. M. Feenstra, J. E. Northrup, and J. Neugebauer, Reconstructions of the AlN(0001) surface, Phys. Rev. B **68**, 205317 (2003).

[42] F. Bernardini, V. Fiorentini, and D. Vanderbilt, Spontaneous polarization and piezoelectric constants of III-V nitrides, Phys. Rev. B **56**, R10024 (1997).

[43] M. Feneberg and K. Thonke, Polarization fields of III-nitrides grown in different crystal orientations, J. Phys.: Condens. Matter **19**, 403201 (2007).

[44] J. Yan, J. J. Mortensen, K. W. Jacobsen, and K. S. Thygesen, Linear density response function in the projector augmented wave method: Applications to solids, surfaces, and interfaces, Phys. Rev. B **83**, 245122 (2011).

[45] A. Ramasubramaniam, Large excitonic effects in monolayers of molybdenum and tungsten dichalcogenides, Phys. Rev. B **86**, 115409 (2012).

[46] Y. Lin, X. Ling, L. Yu, S. Huang, A. L. Hsu, Y.-H. Lee, J. Kong, M. S. Dresselhaus, and T. Palacios, Dielectric screening of excitons and trions in single-layer MoS_2, Nano Lett. **14**, 5569 (2014).

[47] H.-P. Komsa, N. Berseneva, A. V. Krasheninnikov, and R. M. Nieminen, Charged Point Defects in the Flatland: Accurate Formation Energy Calculations in Two-Dimensional Materials, Phys. Rev. X **4**, 031044 (2014).

[48] M. M. Ugeda, A. J. Bradley, S.-F. Shi, F. H. d. Jornada, Y. Zhang, D. Y. Qiu, W. Ruan, S.-K. Mo, Z. Hussain, Z.-X. Shen, F. Wang, S. G. Louie, and M. F. Crommie, Giant bandgap renormalization and excitonic effects in a monolayer transition metal dichalcogenide semiconductor, Nat. Mater. **13**, 1091 (2014).

[49] B. Zhu, X. Chen, and X. Cui, Exciton binding energy of monolayer WS_2, Sci. Rep. **5**, 9218 (2015).

[50] H. J. Liu, J. L. Chen, H. Y. Yu, F. Yang, L. Jiao, G. B. Liu, W. K. Ho, C. L. Gao, J. F. Jia, W. Yao, and M. H. Xie, Observation of intervalley quantum interference in epitaxial monolayer tungsten diselenide, Nat. Commun. **6**, 8180 (2015).

[51] K. F. Mak, C. Lee, J. Hone, J. Shan, and T. F. Heinz, Atomically Thin MoS_2: A New Direct-Gap Semiconductor, Phys. Rev. Lett. **105**, 136805 (2010).

[52] P. Tonndorf, R. Schmidt, P. Böttger, X. Zhang, J. Börner, A. Liebig, M. Albrecht, C. Kloc, O. Gordan, D. R. T. Zahn, S. M. de Vasconcellos, and R. Bratschitsch, Photoluminescence emission and Raman response of monolayer MoS_2, $MoSe_2$, and WSe_2, Opt. Express **21**, 4908 (2013).

[53] A. Chernikov, T. C. Berkelbach, H. M. Hill, A. Rigosi, Y. Li, O. B. Aslan, D. R. Reichman, M. S. Hybertsen, and T. F. Heinz, Exciton Binding Energy and Nonhydrogenic Rydberg Series in Monolayer WS_2, Phys. Rev. Lett. **113**, 076802 (2014).

[54] J. P. Perdew and M. Levy, Physical Content of the Exact Kohn-Sham Orbital Energies: Band Gaps and Derivative Discontinuities, Phys. Rev. Lett. **51**, 1884 (1983).

[55] L. J. Sham and M. Schlüter, Density-Functional Theory of the Energy Gap, Phys. Rev. Lett. **51**, 1888 (1983).

[56] C. S. Wang and W. E. Pickett, Density-Functional Theory of Excitation Spectra of Semiconductors: Application to Si, Phys. Rev. Lett. **51**, 597 (1983).

[57] M. Kuisma, J. Ojanen, J. Enkovaara, and T. T. Rantala, Kohn-sham potential with discontinuity for band gap materials, Phys. Rev. B **82**, 115106 (2010).

[58] T. C. Berkelbach, M. S. Hybertsen, and D. R. Reichman, Theory of neutral and charged excitons in monolayer transition metal dichalcogenides, Phys. Rev. B **88**, 045318 (2013).

[59] M. M. Fogler, L. V. Butov, and K. S. Novoselov, High-temperature superfluidity with indirect excitons in van der waals heterostructures, Nat. Commun. **5**, 4555 (2014).

[60] S. Latini, T. Olsen, and K. S. Thygesen, Excitons in van der waals heterostructures: The important role of dielectric screening, Phys. Rev. B **92**, 245123 (2015).

[61] P. Cudazzo, I. V. Tokatly, and A. Rubio, Dielectric screening in two-dimensional insulators: Implications for excitonic and impurity states in graphane, Phys. Rev. B **84**, 085406 (2011).

[62] L. V. Keldysh, Coulomb interaction in thin semiconductor and semimetal films, JETP Lett. **29**, 658 (1979).

[63] N. A. Lanzillo, N. Kharche, and S. K. Nayak, Substrate-induced Band Gap Renormalization in Semiconducting Carbon Nanotubes, Sci. Rep. **4**, 3609 (2014).

[64] H. M. Hill, A. F. Rigosi, C. Roquelet, A. Chernikov, T. C. Berkelbach, D. R. Reichman, M. S. Hybertsen, L. E. Brus, and T. F. Heinz, Observation of Excitonic Rydberg States in Monolayer MoS_2 and WS_2 by Photoluminescence Excitation Spectroscopy, Nano Lett. **15**, 2992 (2015).

[65] P. R. Gray, P. J. Hurst, S. H. Lewis, and R. G. Meyer, *Analysis and Design of Analog Integrated Circuits*, 5th ed. (Wiley, New York, 2009).

[66] K. K. Kim, A. Hsu, X. Jia, S. M. Kim, Y. Shi, M. Dresselhaus, T. Palacios, and J. Kong, Synthesis and characterization of hexagonal boron nitride film as a dielectric layer for graphene devices, ACS Nano **6**, 8583 (2012).